Article

54Mn radiotracers demonstrate continuous dissolution and reprecipitation of vernadite (#-MnO2) during interaction with aqueous Mn(II)

Evert J. Elzinga

Environ. Sci. Technol., **Just Accepted Manuscript** • DOI: 10.1021/acs.est.6b02874 • Publication Date (Web): 12 Jul 2016

^{54}Mn radiotracers demonstrate continuous dissolution and reprecipitation of vernadite (δ-MnO_2) during interaction with aqueous Mn(II)

Evert J. Elzinga[1*]

[1]Rutgers University

Department of Earth & Environmental Sciences

101 Warren Street

Newark, NJ 07102, USA

*Corresponding author. Email: elzinga@rutgers.edu; phone: (+001)-973-353-5238

ABSTRACT

^{54}Mn radiotracers were used to assess Mn atom exchange between aqueous Mn(II) and vernadite (δ-MnO_2) at pH 5.0. Continuous solid-liquid redistribution of ^{54}Mn atoms occurred, and systems are near isotopic equilibrium after 3 months of reaction. Despite this extensive exchange, XRD and XAS data showed no major changes in vernadite bulk mineralogy. These results demonstrate that the vernadite-Mn(II) interface is dynamic, with the substrate undergoing continuous dissolution-reprecipitation mediated by aqueous Mn(II) without observable impacts on its mineralogy. Interfacial redox reactions between adsorbed Mn(II) and solid-phase Mn(IV) and Mn(III) are proposed as the main drivers of this process. Interaction between aqueous Mn(II) and structural Mn(III) likely involves interfacial electron transfer coupled with Mn atom exchange. The exchange of aqueous Mn(II) and solid-phase Mn(IV) is more complex and is proposed to result from coupled interfacial comproportionation-disproportionation reactions, where electron transfer from adsorbed Mn(II) to lattice Mn(IV) produces transient Mn(III) surface species that disproportionate to re-generate aqueous Mn(II) and structural Mn(IV). These findings provide further evidence for the importance of $Mn(II)_{(aq)}$-$MnO_{2(s)}$ interactions and the attendant production of transient Mn(III) intermediates to the geochemical functioning of phyllomanganates in environments undergoing Mn redox cycling.

INTRODUCTION

The Mn redox cycle influences several important biogeochemical processes, including the cycling of metals and metalloids,[1-10] the degradation of organic molecules,[11-16] and microbial respiration in anaerobic environments.[17-21] The most common Mn-oxides in natural aquatic environments belong to the birnessite family, which is comprised of layered Mn(III, IV)-oxides with octahedral sheets of variable symmetry, layer vacancy density, Mn(III) content, and sheet stacking order.[22-26] Biogeochemical Mn redox cycling often places birnessite minerals in contact with Mn(II)-bearing solutions. The oxidative arm of the cycle is dominated by microbial oxidation of Mn(II) generating birnessite minerals that typically have hexagonal sheet symmetry,[26-42] while on the reductive arm birnessite is reduced by both biotic and abiotic processes that convert Mn(IV) and Mn(III) into Mn(II), resulting in the release and build-up of Mn(II) in solution.[e.g. 18-21, 43-48] Birnessite minerals therefore commonly co-exist and interact with dissolved Mn(II) under both Mn-oxidizing and Mn-reducing conditions.

Interactions between birnessite and aqueous Mn(II) can lead to substantial changes in birnessite structure and composition, because Mn(II) acts as a reductant of structural Mn(IV) inside the mineral lattice.[31-33, 35, 39-41, 49-62] Recent studies suggest that resulting impacts depend on the Mn(II):Mn(IV) ratio, pH, and the presence of metal impurities. At low Mn(II) concentrations (Mn(II):Mn(IV) < 0.5), the content of structural Mn(III) in the birnessite sheets increases,[31-33, 35, 39, 40, 44, 50, 60] whereas at higher concentrations, bulk transformation of birnessite into Mn(III)OOH and $Mn(II)Mn(III)_2O_4$ occurs.[31, 56-59] Bulk transformations are promoted by higher pH values,[57] whereas metal sorbates competing with Mn(II) for surface complexation appear to interfere with the formation of Mn(III)-rich birnessite and secondary MnOOH phases.[39, 50, 58]

In a recent study,[59] we used ^{54}Mn tracers to track the solid-liquid exchange of Mn atoms during the Mn(II)-driven reductive transformation of vernadite, a phyllomanganate with a hexagonal layer structure and limited long-range sheet stacking order.[22, 26] We observed fast exchange of Mn atoms, with isotopic equilibrium reached in 2-4 days, as vernadite transformed into feitknechtite (β-Mn(III)OOH) and manganite (γ-Mn(III)OOH) at pH 7.5. The results from this study suggested that Mn(II) interaction with the vernadite surface triggers the extensive production of short-lived Mn(III) surface species that rapidly undergo disproportionation, and lead to gradual bulk reductive transformation of the δ-MnO_2 substrate through the slow precipitation of MnOOH stabilizing Mn(III). The importance and impacts of transient Mn(III) species in systems without reductive Mn-oxide phase transformations remain to be determined.[59]

The aim of the current study is to assess the extent and dynamics of Mn atom exchange during reaction of dissolved Mn(II) with vernadite under conditions where bulk reductive phase transformations of the phyllomanganate substrate do not occur. Lefkowitz et al.[57] showed that these transformations effectively shut down at pH < 7.0. Experiments were therefore performed at a pH value of 5.0, employing ^{54}Mn radiotracers to track Mn atom exchange across the solid-liquid interface of vernadite, accompanied by X-ray diffraction and X-ray absorption spectroscopy measurements to assess any resulting changes in the mineral structure.

MATERIALS AND METHODS

The materials and methods used here are very similar to those in our earlier study.[59] Natural abundance and ^{54}Mn-labeled vernadite were synthesized based on the method of Gadde and Laitinen.[63] The two materials were prepared from the same starting chemicals, except for the addition of a small ^{54}Mn spike to generate the radiolabeled phase, which had a specific activity

of 498 MBq ^{54}Mn/ mol Mn corresponding to a ^{54}Mn:Mn molar ratio of $1.37*10^{-6}$. The natural abundance and ^{54}Mn-labeled δ-MnO_2 substrates are referred to here as $MnO_{2(s)}$ and $^{54}MnO_{2(s)}$, respectively. Iodine titration [26, 64] of the $MnO_{2(s)}$ sorbent (in triplicate) yielded an average Mn oxidation state of 3.74 (±0.13), indicating the presence of structural Mn(III) as discussed further in section 3.2 of the Supporting Information (SI).

Three types of experiments were conducted: **(1)** sorption of ^{54}Mn-labeled $Mn(II)_{(aq)}$ onto $MnO_{2(s)}$; **(2)** sorption of $Mn(II)_{(aq)}$ onto $^{54}MnO_{2(s)}$); and **(3)** sorption of $Mn(II)_{(aq)}$ onto $MnO_{2(s)}$. The suspensions (100 mL) were prepared in 0.1 M NaCl at a $MnO_{2(s)}$ or $^{54}MnO_{2(s)}$ concentration of 530 µM, corresponding to ~0.05 g L^{-1}, and held in opaque polyethylene containers. The suspensions were spiked with 760 µM of either $Mn(II)_{(aq)}$ or ^{54}Mn-labeled $Mn(II)_{(aq)}$. Suspension pH values were maintained at a value of 5.0 by regular addition of small aliquots of 0.1 M NaOH as necessary. The experiments were run under ambient atmospheric conditions. Exclusion of $O_{2(g)}$ was not deemed necessary based on the results of Lefkowitz et al.[57] who reported that Mn(II) is not sensitive to oxidation by $O_{2(g)}$ in birnessite suspensions at pH ≤ 6.0. The suspensions were sampled regularly over a 3-month time period by filtration of 5 mL subsamples. Supernatants were analyzed for the concentration of dissolved Mn or ^{54}Mn (details below), which were assumed to have an oxidation state of +II based on the low solubility of Mn(IV) and the instability of aqueous Mn(III). As in our earlier study,[59] a series of control samples were prepared and analyzed to constrain data interpretation of the sorption systems. These are described in the SI.

The ^{54}Mn activities in the suspensions of experiments 1 and 2 were identical at 264 kBq L^{-1}. In experiment 2, the activity was determined by the specific activity of the $^{54}MnO_{2(s)}$ substrate (498 MBq ^{54}Mn /mol Mn) and the suspension density of the experiment (530 µM

$^{54}MnO_{2(s)}$). In the suspension of experiment 1, it was set by adding an appropriate amount of $^{54}MnCl_{2(aq)}$ to the 1.0 M $MnCl_{2(aq)}$ stock solution that was introduced into the $MnO_{2(s)}$ suspension to start the experiment. Thus, although the ^{54}Mn activities in the suspensions of experiments 1 and 2 were the same, the initial ^{54}Mn host phases differed: in experiment 1, ^{54}Mn was introduced as aqueous $^{54}Mn(II)$, while in experiment 2, ^{54}Mn started out as solid-phase ^{54}Mn in the $^{54}MnO_{2(s)}$ sorbent.

The supernatants from experiment 3 (which contained no ^{54}Mn) were analyzed for the concentration of dissolved Mn(II) ($[Mn(II)]_{aq}$) using the formaldoxime method.[65] The supernatants from experiments 1 and 2 were analyzed for the concentration of aqueous $^{54}Mn(II)$ ($[^{54}Mn(II)]_{aq}$) using liquid scintillation counting. A 900 µL aliquot of the supernatant was mixed with 5.0 mL of scintillation cocktail (Ecoscint A, National Diagnostics) and counted on a Coulter Beckman LS 6500 to a precision of 0.75% or a maximum counting time of 2 h. The ^{54}Mn solutions and controls from each experiment were counted as a single batch, requiring less than 2 days. Since the half-life of ^{54}Mn is 312.7 days, natural decay of ^{54}Mn during analysis was < 0.5%, which is insignificant relative to the changes in $[^{54}Mn(II)]_{aq}$ resulting from exchange (see results). Sample solids recovered from experiment 3 were analyzed by powder X-ray diffraction (XRD) and synchrotron X-ray absorption spectroscopy (XAS) measurements described in the SI.

RESULTS

Batch kinetic experiments

Figure 1 presents the sorption kinetic results, showing the time dependencies of $[^{54}Mn(II)]_{aq}$ in experiments 1 and 2, and that of $[Mn(II)]_{aq}$ in experiment 3. The results of experiment 1 demonstrate a slow, continuous decline of $[^{54}Mn(II)]_{aq}$ with no evidence to suggest that the

partitioning of ^{54}Mn reaches equilibrium in the 3-month time frame of the experiment. This kinetic pattern is mirrored by the dynamics of ^{54}Mn partitioning in experiment 2, where ^{54}Mn initially is present only in the $^{54}MnO_{2(s)}$ solid. This system exhibits a gradual increase in $[^{54}Mn(II)]_{aq}$ as the $^{54}MnO_{2(s)}$ substrate reacts with aqueous Mn(II), with no evidence to suggest that isotope equilibrium has been reached after 3 months. The kinetic trajectories of the $[^{54}Mn(II)]_{aq}$ levels of experiments 1 and 2 appear to track towards a similar level, suggesting that the solid-liquid partitioning of ^{54}Mn isotopes slowly approaches the same endpoint in both systems. The slow dynamics of ^{54}Mn equilibration in these systems contrast with the rapid attainment of the macroscopic Mn(II) sorption equilibrium in experiment 3, where $Mn(II)_{aq}$ levels stabilize within the first week at ~660 μM (Figure 1). The re-partitioning of ^{54}Mn isotopes in experiments 1 and 2 is therefore not associated with net Mn(II) sorption or desorption, but is driven by Mn atom exchange between the mineral solid and aqueous Mn(II). Results from the control experiments show no release of $^{54}Mn(II)_{aq}$ from the $^{54}MnO_{2(s)}$ substrate in the absence of Mn(II), or during reaction with Zn(II) and Ni(II) (Figure S1). This indicates that the appearance of aqueous $^{54}Mn(II)$ in experiment 2 is not due to $^{54}Mn(II)$-Mn(II) cation exchange at the $^{54}MnO_{2(s)}$ surface. Instead, it is attributed to the interfacial redox reactions between Mn(II) and $^{54}MnO_{2(s)}$ discussed further below.

Quantitative analysis of the experimental results demonstrates extensive exchange of Mn atoms during Mn(II)-vernadite interaction. In experiment 1, ~45% of $^{54}Mn(II)_{(aq)}$ initially in solution has been partitioned to the solid phase after 3 months of reaction (Figure 1). This is equivalent to removal of ~340 μM $^{54}Mn(II)_{(aq)}$, which well exceeds the macroscopic sorption of ~100 μM $Mn(II)_{(aq)}$ measured in experiment 3 (Figure 1). Most of the removal of $^{54}Mn(II)_{(aq)}$ in experiment 1 therefore is due to $Mn(II)_{(aq)}$-$MnO_{2(s)}$ atom exchange. In experiment 2, ~42% of

145 ^{54}Mn initially present in the solid has been mobilized to solution as $^{54}Mn(II)_{(aq)}$ after 3 months of
146 reaction (Figure 1). This release of $^{54}Mn(II)$ contrasts notably with the adsorption of $Mn(II)_{(aq)}$
147 observed macroscopically, again demonstrating the importance of Mn atom exchange between
148 aqueous Mn(II) and the $MnO_{2(s)}$ solid.

149 The extent of exchange can be appreciated by comparing the solid-liquid partitioning of
150 ^{54}Mn and total Mn in these systems. The total Mn concentration in the experiments is 1290 μM,
151 as calculated by summing the concentrations of Mn initially present in the solid (530 μM) and of
152 Mn(II) initially introduced in solution (760 μM). In the equilibrated suspension, $[Mn(II)]_{aq} \approx 660$
153 μM (Figure 1), and the concentration of solid-phase Mn therefore is 1290-660=630 μM. This
154 indicates that approximately half of total Mn is present as solid-phase Mn (630/1290=0.49), and
155 the other half as aqueous $Mn(II)_{(aq)}$. The same solid-liquid distribution is expected for the ^{54}Mn
156 isotopes when the systems are at isotopic equilibrium,[59] and would correspond to an aqueous
157 $^{54}Mn(II)$ level of $[^{54}Mn(II)]_{aq} = 0.51*264 = 135$ kBq L^{-1}. Indeed, the $[^{54}Mn(II)]_{aq}$ levels in both
158 experiments 1 and 2 appear to track towards this predicted endpoint, and are near isotope
159 equilibrium after 3 months (Figure 1). This approach towards Mn exchange equilibrium, which
160 occurs regardless of the original host of ^{54}Mn, indicates that complete mixing of solid-phase and
161 aqueous Mn takes place in these systems. We have previously demonstrated similarly complete
162 Mn isotope solid-liquid exchange during Mn(II)-induced bulk reductive transformation of
163 $MnO_{2(s)}$ into MnOOH at pH 7.5.[59] The XRD and XAS analyses described next assess the
164 structural impacts of Mn atom exchange in the current experiments conducted at pH 5.0.
165
166 *XRD and XAS analyses*

The XRD pattern of $MnO_{2(s)}$ reacted with $Mn(II)_{(aq)}$ for 73 days is compared in Figure 2 to that of the starting substrate and of the vernadite control sample hydrated for 73 days without Mn(II). The patterns are typical of turbostratic vernadite, exhibiting broad *hkl* diffraction bands in the 30°-70° 2θ range, and weak basal reflections at shallower angles (< 30° 2θ). The *hkl* bands, at ~37° 2θ (d = 2.42 Å) and ~66.5° 2θ (d=1.41 Å), dominate the patterns. The positions, shapes and relative intensities of these peaks closely resemble those of earlier studies of vernadite and hexagonal birnessite, and their d-spacings match those of the (11,20) and (31,02) diffraction bands of a C-centered two-dimensional unit cell.[24, 26, 28, 32, 34, 37, 66-69] The hexagonal symmetry of the mineral layers is evident from the value of 1.73 for the ratio of the d values of these bands.[26, 28, 34, 67-69] The faint basal reflection at ~24.5° 2θ demonstrates limited coherence in the stacking of the hexagonal sheets along the c-axis. This is a typical feature of vernadite and indicates a small number of sheets stacked per diffracting particle.[34, 66, 68] Overall, the XRD data demonstrate that turbostratic δ-MnO_2 with hexagonal layer symmetry is the dominant Mn-oxide phase in all three samples.

A detailed inspection of the XRD patterns in Figure 2 reveals subtle differences suggesting structural changes in the $MnO_{2(s)}$ substrate induced by reaction with Mn(II). First, the pattern of Mn(II)-reacted $MnO_{2(s)}$ exhibits a dip at ~46 °2θ in the high-angle scattering tail of the (11,20) peak. This feature has been attributed to the capping of vacancy sites by adsorbed Mn,[28, 34, 44, 67] and has also been observed for vernadite reacted with Ni(II) and Zn(II).[68, 69] Second, the (11,20) and (31,02) peak maxima in the pattern of Mn(II)-reacted $MnO_{2(s)}$ are shifted to slightly lower 2θ relative to the patterns of the original substrate and that of the hydrated control sample (Figure 2). Similar *hkl* band shifts have been observed previously for δ-MnO_2 high in interlayer Mn.[34, 44] Although the exact cause is unknown,[44] possible explanations include a slight expansion

of the unit cell,[34] weak splitting of the (11,20) and (31,02) bands due to incorporation of Mn(III) into the mineral sheets,[59, 60] or a slight increase in particle size.[28, 44] The final change noted for the XRD pattern of Mn(II)-reacted $MnO_{2(s)}$ is the appearance of two small new peaks: one appearing as a shoulder on the (11,02) peak at ~42° 2θ, the other as a weak band at ~56° 2θ (Figure 2). These small bands may be further indications of changes in the δ-MnO_2 lattice or interlayer structure. Grangeon et al.[34] observed a similar shoulder near 42° 2θ in the diffraction pattern of biogenic vernadite, which also contained a broad and weak band near 55° 2θ. These features were successfully reproduced in XRD simulations assuming a relatively large amount of interlayer Mn.[34] Besides modifications of the interlayer, changes in $MnO_{2(s)}$ sheet structure or layer stacking may be involved in the appearance of the new bands as well. Incorporation of Mn(III) into phyllomanganate mineral sheets following oxidation of adsorbed Mn(II) causes splitting of the (11,20) and (31,02) bands, including development of a shoulder at 42° 2θ,[60] while the orientation of layer stacking influences the position and intensity of diffraction bands in the 35°-65° 2θ range.[67] The small additional bands appearing in the pattern of Mn(II)-reacted $MnO_{2(s)}$ thus may signal slight changes in structural Mn(III) content or in the arrangement of sheet stacking.

Another possible explanation for the changes observed in the XRD data is the presence of secondary Mn-oxide(s) formed during Mn(II)-$MnO_{2(s)}$ interaction, although the subtle nature of these changes indicates that any such phases would be present in relatively small amounts. A review of the Powder Diffraction File database of the International Centre for Diffraction Data (ICDD)[70] revealed several known Mn-oxide minerals with characteristic peaks near 42° and 55° 2θ, including pyrolusite (β-MnO_2) and nsutite (γ-MnO_2). However, these phases all have additional diagnostic high-intensity diffraction peaks that are absent in the XRD pattern of the

Mn(II)-reacted sample. This suggests that modification of the vernadite interlayer or layer structure (as discussed above) is the more likely cause of the subtle changes in the XRD pattern of the Mn(II)-reacted material.

The Mn *K*-edge XAS data presented in Figure 3 and SI Figures S2-S4 help further constrain the structural impacts of aqueous Mn(II) on the $MnO_{2(s)}$ substrate. The near-edge spectrum of Mn(II)-reacted $MnO_{2(s)}$ is similar to that of the starting substrate and the control sample (Figure S3), indicating similar Mn mineralogy. Net sorption of $Mn(II)_{(aq)}$ is reflected in increased spectral intensity at 6.545-6.560 keV in the spectrum of Mn(II)-reacted $MnO_{2(s)}$ (Figure S3). The k^3-weighted χ-spectra of the $MnO_{2(s)}$ samples are displayed in Figure 3a, and the corresponding raw and fitted Fourier transform functions are shown Figure 3b; the fit results are summarized in Table S1. The χ spectra have similar frequencies (Figure 3a), indicating that the $MnO_{2(s)}$ samples have similar structures, in agreement with the XRD data (Figure 2). This is confirmed by the similarity of the radial structure functions (Figure 3b) and fit results (Table S1), which are consistent with previous EXAFS fits of vernadite.[28, 34] The main difference is a reduction in amplitude of the oscillations in the spectrum of Mn(II)-reacted $MnO_{2(s)}$ relative to that of the other samples, as demonstrated particularly well by the overlay of χ spectra presented in Figure S4. This dampening is manifested in the radial structure function by the reduced intensities of the Fourier transform peaks (Figure 3b), and in the fit results by lower coordination numbers and/or higher Debye-Waller factors of the Mn-O and Mn-Mn shells (Table S1). Villalobos et al.[28] and Grangeon et al.[34] noted similar oscillation dampening in the EXAFS spectra of Mn(II, III)-rich biogenic phyllomanganates. This likely arises from structural disorder effects induced by the variability of Mn-O and Mn-Mn distances with Mn oxidation state.[28, 34] Some dampening also occurs in the χ spectrum of the hydrated control sample relative to the

original $MnO_{2(s)}$ material (Figures 3 and S4; Table S1), suggesting slight changes in Mn speciation induced by hydration and aging of the $MnO_{2(s)}$ suspension. The exact cause and nature of these changes cannot be determined from the current data, although one may speculate that repartitioning of structural or interlayer Mn(III) is involved. Additional work is required to investigate these effects in more detail.

Besides oscillation dampening, no other major differences are visible in the EXAFS data of Mn(II)-reacted $MnO_{2(s)}$ versus the other samples (Figures 3 and S4; Table S1). This confirms that the phyllomanganate sheet structure remains intact during long-term interaction with $Mn(II)_{(aq)}$ under the conditions of this study, and indicates that the $MnO_{2(s)}$ substrate does not undergo major changes in bulk mineralogy, consistent with the XRD results (Figure 2). This lack of change in $MnO_{2(s)}$ bulk structure is notable in view of the ^{54}Mn results presented in Figure 1, which suggest that full exchange occurs between solid-phase and aqueous Mn (see discussion in previous section). It also is a distinct and notable difference with our previous study conducted at pH 7.5, where ^{54}Mn isotope equilibration occurred concurrent with bulk mineralogical transformation of $MnO_{2(s)}$ into Mn(III)OOH phases.[59] The mechanistic interpretations and implications of these findings are discussed next.

Mechanisms of Mn atom exchange

The combined results of the ^{54}Mn radiotracer experiments and the structural analyses demonstrate that $MnO_{2(s)}$ is dynamic in the presence of $Mn(II)_{(aq)}$. The mineral substrate is engaged in continuous reactions exchanging aqueous Mn(II) and solid-phase Mn without undergoing phase changes. This "swapping" of Mn atoms between the aqueous and solid phase cannot be observed macroscopically through changes in $[Mn(II)]_{aq}$, as shown by the results of

experiment 3 in Figure 1. This indicates the establishment of a dynamic equilibrium between $MnO_{2(s)}$ dissolution (which involves conversion of solid-phase Mn into aqueous Mn(II)) and $MnO_{2(s)}$ precipitation (conversion of aqueous Mn(II) into solid-phase Mn), where the fluxes of Mn between the solid and liquid phase are at steady state. The interaction of $MnO_{2(s)}$ with aqueous Mn(II) thus induces a continuous recrystallization of the mineral substrate without causing bulk structural changes in the $MnO_{2(s)}$ substrate .

The average oxidation state of the $MnO_{2(s)}$ starting sorbent is ~3.74, indicating that it contains a considerable fraction (~26%) of structural and interlayer Mn(III) (see discussion in SI). The heterogeneity of solid-phase Mn valence implies that exchange with aqueous Mn(II) proceeds through different pathways that vary with Mn oxidation state. Since Mn(IV) is the dominant solid-phase Mn species, $Mn(IV)_{(s)}$-$Mn(II)_{(aq)}$ atom exchange predominates. Exchange of lattice $^{54}Mn(IV)$ can be summarized as:

$$Mn(II)_{(aq)} + {}^{54}Mn(IV)_{(s)} \leftrightarrow {}^{54}Mn(II)_{(aq)} + Mn(IV)_{(s)}. \quad (1)$$

Mechanistically, this reaction likely involves coupled comproportionation-disproportionation reactions at the $MnO_{2(s)}$ surface, as discussed in our previous study.[59] The process is initiated by interfacial electron transfer from adsorbed Mn(II) to lattice Mn(IV), which produces transient Mn(III) species that disproportionate to re-form aqueous Mn(II) and solid phase Mn(IV).[59] An example of a specific pathway is interfacial $^{54}Mn(IV)$-Mn(II) comproportionation generating transient $^{54}Mn(III)$ species (denoted as $>{}^{54}Mn(III)$) that disproportionate to form $^{54}Mn(II)_{(aq)}$:

$$Mn(II)_{(aq)} + {}^{54}Mn(IV)_{(s)} \leftrightarrow >Mn(III) + >{}^{54}Mn(III) \leftrightarrow Mn(IV)_{(s)} + {}^{54}Mn(II)_{(aq)} \quad (2)$$

yielding reaction (1). Other pathways of coupled comproportionation-disproportionation can be envisioned. For instance, >Mn(III) produced by interfacial Mn(II)-Mn(IV) comproportionation may disproportionate with structural Mn(III) of the $MnO_{2(s)}$ starting substrate, or lattice $^{54}Mn(IV)$

may react with two aqueous Mn(II) atoms to form aqueous Mn and two >Mn(III) atoms that subsequently undergo disproportionation. It is likely that these and other pathways of Mn(II)-Mn(IV) exchange, mediated by transient Mn(III), operate simultaneously to drive vernadite recrystallization.

Interaction of aqueous Mn(II) with solid-phase ^{54}Mn(III) may lead to Mn atom exchange through interfacial electron transfer according to:[59]

$$^{54}Mn(III)_{(s)} + Mn(II)_{(aq)} \leftrightarrow {}^{54}Mn(II)_{(aq)} + Mn(III)_{(s)}. \quad (3)$$

Such coupled electron transfer and atom exchange reactions between solid-phase Mn(III) and aqueous Mn(II) were proposed by Elzinga[56] to explain Mn(II)-catalyzed conversion of metastable feitknechtite (β-MnOOH) into manganite (γ-MnOOH), and were recently proposed to explain oxygen isotope exchange between manganite and solutions containing $Mn(II)_{(aq)}$.[71] The Mn(II)-Mn(III) exchange described by reaction 3 may couple with Mn(II)-Mn(IV) exchange described by reaction 1. This would occur if Mn(III) produced by interfacial Mn(II)-Mn(IV) comproportionation (reaction 2) engages in electron transfer and atom exchange with aqueous Mn(II).

A final pathway to consider is homovalent exchange between aqueous Mn(II) and solid-phase ^{54}Mn(II), described by:

$$^{54}Mn(II)_{(s)} + Mn(II)_{(aq)} \leftrightarrow {}^{54}Mn(II)_{(aq)} + Mn(II)_{(s)}. \quad (4)$$

The results of the Ni(II)- and Zn(II)-$^{54}MnO_{2(s)}$ sorption experiments (Figure S1) suggest that exchangeable ^{54}Mn(II) is a minor species at the surface of the $^{54}MnO_{2(s)}$ starting substrate, as noted earlier. Moreover, ion exchange is a rapid mechanism that typically equilibrates on a time scale of minutes to hours,[72] while ^{54}Mn isotope equilibration in the current experiments requires

> 3 months (Figure 1). The interfacial redox processes defined by reactions 1 and 3 are therefore most relevant to the solid-liquid exchange of Mn observed here.

Our previous study of ^{54}Mn exchange employed identical $MnO_{2(s)}$ and $Mn(II)_{(aq)}$ concentrations as used here, but was conducted at pH 7.5 instead of pH 5.0.[59] This pH difference has a tremendous impact on the rate of ^{54}Mn solid-liquid exchange, with Mn isotope equilibrium reached within 4 days at pH 7.5 [59] while the equilibration time required in the current experiments conducted at pH 5.0 is > 3 months (Figure 1). In the pH 7.5 study, vernadite underwent bulk reductive transformation into MnOOH according to:

$$Mn^{2+}_{(aq)} + Mn(IV)O_{2\,(s)} + 2\,H_2O \leftrightarrow 2\,Mn(III)OOH_{(s)} + 2\,H^{+}_{(aq)} \quad (5)$$

This bulk phase change, which went to completion within four days in this earlier study,[59] is expected to promote ^{54}Mn isotope equilibration as it enables extensive solid-fluid interaction and likely involves dissolution of $MnO_{2(s)}$ and reprecipitation as secondary $MnOOH_{(s)}$. It does not occur in the current experiments (Figure 2) because it is thermodynamically unfavorable at pH 5.0 at the aqueous Mn(II) level used here.[57] This slows down ^{54}Mn isotope exchange at pH 5.0 relative to pH 7.5 in these systems. A second factor is in play as well. In the pH 7.5 experiments, we observed that >75% of the structural Mn atoms in vernadite had exchanged in the first 2 hours of reaction before nucleation of secondary $MnOOH_{(s)}$ phases was observed.[59] This suggests recrystallization of the vernadite starting solid as a major cause of ^{54}Mn redistribution during the early stages of reaction at pH 7.5, proceeding at a rate much faster than observed here at pH 5.0 (Figure 1). The most plausible explanation for this pH effect is that the adsorption of Mn(II) onto the $MnO_{2(s)}$ surface, a step critical to initiate interfacial Mn(II)-Mn(IV) comproportionation, is more favorable at higher pH due to reduced competition by protons for inner-sphere surface complexation.[73] This would allow for more extensive Mn(II)-$MnO_{2(s)}$

interaction speeding up vernadite dissolution-reprecipitation at higher pH. This finding additionally suggests that at pH 7.5 the rate and extent of Mn(III) production through interfacial comproportionation well exceeds the stabilization of Mn(III) through formation of $MnOOH_{(s)}$ during the early stages of Mn(II)-$MnO_{2(s)}$ interaction. As a result, Mn(III) is not stabilized, but instead undergoes disproportionation to drive recrystallization of the vernadite solid. The gradual nucleation of secondary $MnOOH_{(s)}$ stabilizing Mn(III) ultimately causes bulk reductive transformation of the $MnO_{2(s)}$ substrate at pH 7.5.[56-59] At the lower pH value of 5.0 studied here, precipitation of Mn(III) phases does not occur (Figure 2) due to the lack of thermodynamic favorability under the reaction conditions applied, as noted above. The absence of a mechanism stabilizing Mn(III) formed through interfacial Mn(II)-Mn(IV) comproportionation explains why the $MnO_{2(s)}$ substrate undergoes continuous recrystallization at this lower pH value.

The main finding of the current study is that the interaction of aqueous Mn(II) with vernadite at pH 5.0 leads to continuous Mn(II)-driven dissolution-reprecipitation of the vernadite substrate, without major changes in its mineralogical form. Such recrystallization processes have not been previously observed for phyllomanganates, but have been demonstrated during interaction of Fe(III)-oxides with aqueous Fe(II).[74-79] However, the exchange processes are not equivalent in the Mn and Fe systems. This is because Fe(III)-oxide recrystallization involves direct Fe(II)-Fe(III) electron exchange reactions, while that of $MnO_{2(s)}$ predominantly involves Mn(II)-Mn(IV) exchange presumably with formation of transient Mn(III) intermediates. The mechanisms of Mn solid-liquid exchange and the resulting impacts on Mn-oxide structure, morphology and reactivity require further study.

ENVIRONMENTAL IMPLICATIONS

The results from this study provide, for the first time, direct evidence for Mn atom exchange between aqueous Mn(II) and vernadite without concurrent mineralogical phase transformations. These findings indicate that aqueous Mn(II) drives continuous dissolution and reprecipitation of the phyllomanganate substrate. Hexagonal phyllomanganates are important mineral regulators of the distribution and speciation of trace metals in terrestrial and marine environments.[e.g. 4-10] The dynamic nature of the $MnO_{2(s)}$-$Mn(II)_{(aq)}$ interface implies that metal adsorbates may be subject to substantial changes in partitioning and speciation during Mn(II)-driven dissolution and re-precipitation of the mineral sorbent, as observed for the Fe(III)-oxides.[76- 78] An important additional implication is the formation of transient Mn(III) surface species through interfacial Mn(II)-Mn(IV) comproportionation as the main driver of Mn atom exchange. These Mn(III) species may impact the adsorption and redox reactivity of the $MnO_{2(s)}$ substrate by engaging in complexation,[54, 57] redox,[80-85] or competitive interactions[50, 57, 86] with metal(loid) sorbates, and may be a source of dissolved Mn(III).[49, 87-90] The results from this study thus have important implications for the cycling of Mn and trace metals in aqueous environments where phyllomanganates are in contact with dissolved Mn(II). This scenario is common in settings such as suboxic riparian soils, the redox-clines of stratified marine and lake water columns, and aquifers impacted by acid mine drainage. The combined results of the current study conducted at pH 5.0 and previous studies performed at pH > 7 [56-59] demonstrate the importance of pH as a control on the impacts of $Mn(II)_{(aq)}$-$MnO_{2(s)}$ interaction. At neutral pH and higher, Mn(III) produced through interfacial comproportionation may precipitate as secondary Mn(III)-hydroxide minerals[56-59] or be stabilized by incorporation into the phyllomanganate sheets,[60] whereas at lower pH values these Mn(III) species drive recrystallization of the $MnO_{2(s)}$ substrate without inducing observable structural changes, as shown by the current data. Effects of aqueous

Mn(II) on Mn-oxide geochemistry will thus be quite different in marine environments (pH~8.3) and suboxic soils (pH~7) than in acid mine drainage systems. Further work is needed to elucidate the dynamics and processes of $Mn(II)_{(aq)}$-$MnO_{2(s)}$ interaction and resulting impacts on the biogeochemical cycling of Mn and trace metal(loid)s.

SUPPORTING INFORMATION AVAILABLE

Description of: (1) the control experiments; (2) the XRD measurements; (3) the Mn *K*-edge XAS measurements and analyses of the $MnO_{2(s)}$ samples, including assessment of the Mn oxidation state based on near-edge spectra.

ACKNOWLEDGMENTS

Funding for this work was provided by Rutgers University. Use of the Bruker D8 Advance X-ray diffractometer at Rutgers-Newark was supported by the NSF through award EAR-1337450. I thank Adam Kustka for use of the radio-isotope facility at Rutgers-Newark, and Sungsik Lee and Ben Reinhart at APS beamline 12BMB-B for assistance during XAS data collection. I would also like to thank Daniel Giammar and six anonymous reviewers for their constructive and insightful comments that improved this paper.

REFERENCES

(1) Borch, T.; Kretzschmar, R.; Kappler, A.; Cappellen, P. Van; Ginder-Vogel, M.; Voegelin, A.; Campbell, K. Biogeochemical redox processes and their impact on contaminant dynamics. *Environ. Sci. Technol.* **2010**, *44*, 15–23.

(2) Fuller, C.C.; Bargar, J.R. Processes of zinc attenuation by biogenic manganese oxides forming in the hyporheic zone of Pinal Creek, Arizona. *Environ. Sci. Technol.* **2014**, 48, 2165-2172.

(3) Manceau, A.; Lanson, B.; Schlegel, M. L.; Harge, J. C.; Musso, M.; Eybert-Berard L, Hazemann, J. L.; Chateigner, D., Lamble, G. M. Quantitative Zn speciation in smelter-contaminated soils by EXAFS spectroscopy. *Geochim. Cosmochim. Acta* **2000**, 66, 2639-2663.

(4) Peacock, C. L.; Sherman, D. M. Sorption of Ni by birnessite: Equilibrium controls on Ni in seawater. *Chem. Geol.* **2007**, 238, 94−106.

(5) Toner, B.; Manceau, A.; Webb, S. M.; Sposito, G. Zinc sorption to biogenic hexagonal-birnessite particles within a hydrated bacterial biofilm. *Geochim. Cosmochim. Acta* **2006**, 70, 27−43.

(6) Marcus, M. A.; Manceau, A.; Kersten, M. Mn, Fe, Zn and As speciation in a fast-growing ferromanganese marine nodule. *Geochim. Cosmochim. Acta* **2004**, 68, 3125-3136.

(7) Peacock, C. L.; Moon, E. M., Oxidative scavenging of thallium by birnessite: Explanation for thallium enrichment and stable isotope fractionation in marine ferromanganese precipitates. *Geochimica et Cosmochimica Acta* **2012,** *84*, 297-313.

(8) Manceau, A.; Tamura, N.; Celestre, R. S.; MacDowell A. A.; Geoffroy N.; Sposito, G.; Padmore, H. A. Molecular-scale speciation of Zn and Ni in soil ferromanganese nodules from loess soils of the Mississippi basin. *Environ. Sci. Technol*. **2003**, **37,** 75–80.

(9) Oze, C.; Bird, D.K.; Fendorf, S. Genesis of hexavalent chromium from natural sources in soil and groundwater. *Proc. Natl. Acad. Sci. U.S.A.* **2007**, 104, 6544-6549.

(10) O'Reilly, S. E.; Hochella, M. F. Lead sorption efficiencies of natural and synthetic Mn and Fe-oxides, *Geochim. Cosmochim. Acta* **2003**, 67, 4471-4487.

(11) Stone A.T.; Morgan J.J. Reduction and dissolution of manganese(III) and manganese(IV) oxides by organics. 2. Survey of the reactivity of organics. *Environ. Sci. Technol* **1984**, 18, 617-624.

(12) Matocha C.J.; Sparks D.L.; Ammonette J.W.; Kukkadapu R.K. Kinetics and mechanism of birnessite reduction by catechol. *Soil Sci. Soc.Am.J.* **2001**, 65, 58-66.

(13) Banerjee D.; Nesbitt H.W. XPS study of dissolution of birnessite by humate with constraints on reaction mechanism. *Geochim. Cosmochim. Acta* **2001**, 65, 1703–1714.

(14) Sunda ,W.G.; Kieber, D.J. Oxidation of humic substances by manganese oxides yields low-molecular-weight organic substrates. *Nature* **1994**, 367, 62–64.

(15) Stone A.T. Microbial metabolites and the reductive dissolution of manganese oxides: Oxalate and pyruvate. *Geochim. Cosmochim.Acta* **1987**, 51, 919–925.

(16) Banerjee, D.; Nesbitt W. XPS study of reductive dissolution of birnessite by oxalate: rates and mechanistic aspects of dissolution and redox processes. *Geochim. Cosmochim. Acta* **1999**, 63, 3025–3038.

(17) Nealson, K.H.; Saffarini, D. Iron and manganese in anaerobic respiration: Environmental significance, physiology, and regulation. *Annual Rev. Microbiol.* **1994**, 48, 311-343.

(18) Fischer, T.B.; Heaney, P.J.; Ross, D.E.; Brantley, D.L.; Post, J.E.; Tien, M. Continuous time-resolved X-ray diffraction of the biocatalyzed reduction of Mn oxide. *Am. Mineral*. **2008**, 93, 1929-1932.

(19) Lin, H.; Szeinbaum, N.H.; DiChristina, T.J.; Taillefert, M. 2012. Microbial Mn(IV) reduction requires an initial one-electron reductive solubilization step. *Geochim. Cosmochim. Acta* **2012**, 99, 179−192.

(20) Ehrlich, H.L. Manganese oxide reduction as a form of anaerobic respiration. G*eomicrobiol. J*. **1987**, 5, 423−431.

(21) Weber, F.A.; Voegelin, A.; Kretzschmar, R. Multi-metal contaminant dynamics in a temporarily flooded soil under sulfate limitation. *Geochim. Cosmochim. Acta* **2009**, 73, 5513-5527.

(22) Post J. E. Manganese oxide minerals: Crystal structures and economic and environmental significance. *Proc. Natl. Acad. Sci. U. S. A.*, **1999,** 96, 3447-3454.

(23) Silvester, E.; Manceau, M.; and Drits, V. A. Structure of synthetic monoclinic Na-rich birnessite and hexagonal birnessite: II. Results from chemical studies and EXAFS spectroscopy. *Am. Mineral.* **1997**, *82*, 962-978.

(24) Drits, V. A.; Silvester, E.; Gorshkov, A. I.; and Manceau, A. Structure of synthetic monoclinic Na-rich birnessite and hexagonal birnessite: I. Results from X-ray diffraction and selected-area electron diffraction. *Am. Mineral.* **1997**, *82*, 946-961.

(25) Lanson, B.; Drits, V. A.; Silvester, E.; and Manceau, A. Structure of H-exchanged hexagonal birnessite and its mechanism of formation from Na-rich monoclinic buserite at low pH. *Am. Mineral.* **2000**, *85*, 826-838.

(26) Villalobos, M.; Toner, B.; Bargar, J. R.; Sposito, G. Characterization of the manganese oxide produced by *Pseudomonas putida* strain MnB1. *Geochim. Cosmochim. Acta* **2003**, 67, 2649-2662.

(27) Tebo, B. M.; Bargar, J. R.; Clement, B. G.; Dick, G. J.; Parker, D.; Verity, R.; Webb S. M. Biogenic manganese oxides: Properties and mechanisms of formation. *Annu. Rev. Earth Planet. Sci.* **2004,** 32, 287-328.

(28) Villalobos, M.; Lanson, B.; Manceau, A.; Toner, B.; Sposito, G. Structural model for the biogenic Mn oxide produced by Pseudomonas putida. *Am. Mineral.* **2006**, *91*, 489-502.

(29) Spiro, T. G.; Bargar, J. R.; Sposito, G.; Tebo, B.M. Bacteriogenic manganese oxides. *Acc. Chem. Res.* **2010**, 43, 2-9.

(30) Learman D. R.; Voelker B. M.; Vazquez-Rodriguez, A. I.; Hansel, C. M. Formation of manganese oxides by bacterially generated superoxide. *Nat. Geosci.* **2011,** 4, 95-98.

(31) Bargar, J. R.; Tebo, B. M.; Bergmann, U.; Webb, S. M.; Glatzel, P.; Chiu V. Q.; Villalobos, M. Biotic and abiotic products of Mn(II) oxidation by spores of the marine *Bacillus sp.* strain SG-1. *Am. Mineral*. **2005**, 90, 143-154.

(32) Webb, S. M.; Tebo, B. M.; Bargar, J. R. Structural characterization of biogenic Mn oxides produced in seawater by the marine *bacillus sp.* strain SG-1. *Am. Mineral.* **2005**, 90, 1342-1357.

(33) Santelli, C. M.; Webb, S. M.; Dohnalkova, A. C.; Hansel C. M. Diversity of Mn oxides produced by Mn(II)-oxidizing fungi. *Geochim. Cosmochim. Acta* **2011**, 75, 2762-2776.

(34) Grangeon, S.; Lanson, B.; Miyata N.; Tani, Y.; Manceau, A. Structure of nanocrystalline phyllomanganates produced by freshwater fungi. *Am. Mineral*. **2010**, 95, 1608-1616.

(35) Learman, D. R.; Wankel, S.D.; Webb, S.M.; Martinez, N.; Madden, A. S.; Hansel, C. M. Coupled biotic-abiotic Mn(II) oxidation pathway mediates the formation and structural evolution of biogenic Mn oxides. *Geochim. Cosmochim. Acta* **2011**, 75, 6048-6063.

(36) Hansel, C. M.; Zeiner, C. A.; Santelli, C. M.; Webb, S.M. Mn(II) oxidation by an ascomycete fungus is linked to superoxide production during asexual reproduction. *Proc. Natl. Acad. Sci. U. S. A.* **2012**, 109, 12621-12625.

(37) Jurgensen, A.; Widmeyer, J. R.; Gordon, R. A.; Bendell-Young, L. I.; Moore, M. M.; Crozier, E. D. The structure of the manganese oxide on the sheath of the bacterium Leptothrix discophora: An XAFS study. *Am. Mineral.* **2004**, 89, 1110–1118.

(38) Saratovsky, I.; Wightman, P. G.; Pasten, P. A.; Gaillard, J. F.; Poeppelmeier, K. R. Manganese oxides: Parallels between abiotic and biotic structures. *J. Am. Chem. Soc.* **2006**, 128, 11188-11198.

(39) Frierdich, A.J.; Hasenmueller, E.A.; Catalano, J.G. Composition and structure of nanocrystalline Fe and Mn oxide cave deposits: Implications for trace element mobility in karst systems. *Chem. Geol.* **2011***,* 284, 82-96..

(40) Bargar, J.R.; Fuller, C.C.; Marcus, M.A.; Brearley, A.J.; De la Rosa, M.P.; Webb, S.M.; Caldwell, W.A. Structural characterization of terrestrial microbial Mn oxides from Pinal Creek, AZ. *Geochim. Cosmochim. Acta* **2009***,* 73, 889-910.

(41) Mandernack, K.W.; Post, J.; Tebo, B.M. Manganese mineral formation by bacterial spores of the marine Bacillus, strain SG- 1: Evidence for the direct oxidation of Mn(II) to Mn(IV). *Geochim. Cosmochim. Acta* **1995**, 59, 4393–4408.

(42) Droz, B.; Dumas, N.; Duckworth, O.W.; Pena, J. A comparison of the sorption reactivity of bacteriogenic and mycogenic Mn oxide nanoparticles. *Environ. Sci. Technol.* **2015**, 49, 4200-4208.

(43) Lafferty, B.M.; Ginder-Vogel, M.; Sparks, D.L. Arsenite oxidation by a poorly crystalline manganese oxide 1. Stirred flow experiments. *Environ. Sci. Technol.* **2010**, 44, 8460-8466.

(44) Lafferty, B.M.; Ginder-Vogel, M.; Zhu, M.; Livi, K.J.T.; Sparks, D.L. Arsenite oxidation by a poorly crystalline manganese oxide 2. Results from X-ray absorption spectroscopy and X-ray diffraction. *Environ. Sci. Technol.* **2010**, 44, 8467-8472.

(45) Parikh, S.J.; Lafferty, B.J.; Sparks, D.L. An ATR-FTIR spectroscopic approach for measuring rapid kinetics at the mineral/water interface. *J. Collloid Interface Sci*. **2008**, 320, 177-185.

(46) Landrot, G.; Ginder-Vogel, M.; Livi, K.; Fitts, J.P.; Sparks, D.L. Chromium(III) oxidation by three poorly-crystalline manganese(IV) oxides. 1. Chromium(III)-oxidizing capacity. *Env. Sci. Technol.* **2012**, 46, 11594-11600.

(47) Postma, D.; Appelo, C.A.J. Reduction of Mn-oxides by ferrous iron in a flow system: Column experiment and reactive transport modeling. *Geochim. Cosmochim. Acta* **2000**, 64, 1237-1247.

(48) Fendorf, S.; Jardine, P.M.; Patterson, R.R.; Taylor, D.L.; Brooks, S.C. Pyrolusite surface transformations measured in real-time during the reactive transport of Co(II)EDTA^{2-}. *Geochim. Cosmochim. Acta* **1999**, 63, 3049–3057.

(49) Webb, S.M.; Dick, G.J.; Bargar, J.R.; Tebo, B.M. Evidence for the presence of Mn(III) intermediates in the bacterial oxidation of Mn(II). *Proc. Natl. Acad. Sci. U. S. A.* **2005**, 102, 5558−5563.

(50) Zhu, M.; Ginder-Vogel, M.; Parikh, S.J.; Feng, X.H.; Sparks, D.L. Cation effects on the layer structure of biogenic Mn-oxides. *Environ. Sci. Technol.* **2010**, 44, 4465-4471.

(51) Perez-Benito, J. F. Reduction of colloidal manganese dioxide by manganese(II). *J. Colloid Interface Sci*. **2002**, 248, 130−135.

(52) Tu, S.; Racz, G. J.; Goh, T. B. Transformations of synthetic birnessite as affected by pH and manganese concentration. *Clays Clay Minerals* **1994**, 42, 321−330.

(53) Feng, X. H.; Zhu, M.; Ginder-Vogel, M.; Nic, C.; Parikh, S. J.; D. L. Sparks. Formation of nano-crystalline todorokite from biogenic Mn oxides. *Geochim. Cosmochim. Acta*. **2010**, 74, 3232-3245.

(54) Chang, J. N.; Tani, Y.; Naitou, H.; Miyata, N.; Tojo F.; Seyama, H. Zn(II) sequestration by fungal biogenic manganese oxide through enzymatic and abiotic processes. *Chem. Geol*. **2014**, 383, 155-163.

(55) Atkins, A. L.; Shawn, S.; Peacock, C. L. Nucleation and growth of todorokite from birnessite: Implications for trace metal cycling in marine sediments. *Geochim.Cosmochim. Acta.* **2014**, 144, 109-125.

(56) Elzinga, E. J. Reductive transformation of birnessite by aqueous Mn(II). *Environ. Sci. Technol*. **2011**, 45, 6366−6372.

(57) Lefkowitz, J. P.; Rouff, A. A.; Elzinga, E. J. Influence of pH on the reductive transformation of birnessite by aqueous Mn(II). *Environ. Sci. Technol*. **2013,** 47, 10364-10371.

(58) Lefkowitz, J.P.; Elzinga, E.J. Impacts of aqueous Mn(II) on the sorption of Zn(II) by hexagonal birnessite. *Environ. Sci. Technol*. **2015,** 49, 4886-4893.

(59) Elzinga, E.J.; Kustka, A.B. A Mn-54 radiotracer study of Mn Isotope solid−liquid exchange during reductive transformation of vernadite (δ-MnO_2) by aqueous Mn(II). *Environ. Sci. Technol*. **2015,** 49, 4310-4316.

(60) Zhao, H.; Zhu, M.; Li, W.; Elzinga, E.J.; Villalobos, M.; Liu, F.; Zhang, J.; Feng, X.; Sparks, D.L. Redox reactions between Mn(II) and hexagonal birnessite change it layer symmetry. *Environ. Sci. Technol.* **2016**, 50, 1750-1758.

(61) Ehlert, K.; Mikutta, C.; Kretzschmar, R. Impact of birnessite on arsenic and iron speciation during microbial reduction of arsenic-bearing ferrihydrite. *Environ. Sci. Technol.* **2014**, 48, 11320-11329.

(62) Johnson, J.E.; Savalia, P.; Davis, R.; Kocar, B.D.; Webb, S.M.; Nealson, K.H.; Fischer, W.W. Real-time manganese phase dynamics during biological and abiotic manganese oxide reduction. *Environ. Sci. Technol.* **2016**, 50, 4248-4258.

(63) Gadde, R.R.; Laitinen, H.A. Heavy metal adsorption by hydrous iron and manganese oxides. Anal. Chem. **1974**, 46, 2022-2026.

(64) Murray, J. W.; Balistrieri, L. S.; Paul, B. The oxidation-state of manganese in marine-sediments and ferromanganese nodules. *Geochim. Cosmochim. Acta* **1984**, *48*, 1237–1247.

(65) Burle, E.; Kirby-Smith, W.W. Application of formaldoxime colorimetric method for the determination of manganese in the pore water of anoxic estuarine sediments. *Estuaries Coasts* **1979**, 2, 198-201.

(66) Lanson, B.; Marcus, M. A.; Fakra, S.; Panfili, F.; Geoffroy, N.; Manceau, A. Formation of Zn-Ca phyllomanganate nanoparticles in grass roots. *Geochim. Cosmochim. Acta.* **2008**, 72, 2478-2490.

(67) Drits, V. A.; Lanson, B.; Gaillot, A.C. Birnessite polytype systematics and identification by powder X-ray diffraction. *Am. Mineral.* **2007**, 92, 771-788.

(68) Grangeon, S.; Lanson, B.; Lanson, M.; Manceau, A. Crystal structure of Ni-sorbed synthetic vernadite: A powder X-ray diffraction study. *Mineralogical Magazine*, **2008**, 72, 1279–1291

(69) Grangeon, S.; Manceau A.; Guilhermet, J.; Gaillot, A.C.; Lanson, M.; Lanson B. Zn sorption dynamically modifies the layer and interlayer structure of vernadite. *Geochim. Cosmochim. Acta* **2012**, 85, 302-313.

(70) Faber, J.; Fawcett, T. The Powder Diffraction File: Present and future. *Acta Cryst.* **2002**, *B58*, 325-332

(71) Frierdich, A.J.; Spicuzza, M.J.; Scherer, M.M. Oxygen isotope evidence for Mn(II)-catalyzed recrystallization of manganite (γ-MnOOH). *Environ. Sci. Technol.* DOI**:** 10.1021/acs.est.6b01463.

(72) Sparks, D.L. 1999. Kinetics and mechanisms of chemical reactions at the soil mineral/water interface. p. 135-192 *In:* D.L. Sparks (ed). Soil Physical Chemistry, 2nd edition. CRC Press, Boca Raton, FL.

(73) Sparks, D. L. Toxic metals in the environment: The role of surfaces. *Elements* **2005**, *1*, 193-197.

(74) Handler, R.M.; Beard, B.L.; Johnson, C.M.; Scherer, M.M. Atom exchange between aqueous Fe(II) and goethite: an Fe isotope tracer study. *Environ. Sci. Technol.* **2009**, *43*, 1102-1107.

(75) Rosso, K.M.; Yanina, S.V.; Gorski, C.A.; Larese-Casanova, P.; Scherer, M.M. Connecting observations of hematite (α-Fe_2O_3) growth catalyzed by Fe(II). *Environ. Sci. Technol*, **2010***,* 44, 61–67.

(76) Frierdich, A.J.; Luo, Y.; Catalano, J.G. Trace element cycling through iron oxide minerals during redox-driven dynamic recrystallization. *Geology* **2011**, *39*, 1083-1086.

(77) Frierdich, A.J.; Catalano J.G. Controls on Fe(II)-activated trace element release from goethite and hematite. *Environ. Sci. Technol.* **2012**, *46*, 1519-1526.

(78) Latta, D.E.; Gorski, C.A.; Scherer, M.M. Influence of Fe^{2+}-catalysed iron oxide recrystallization on metal cycling. *Biogeochem. Soc. Transactions* **2012**, 40, 1191-1197.

(79) Handler, R.M; Frierdich, A.J.; Johnson C.M.; Rosso, K.M.; Beard, B.L.; Wang, C.; Latta, D.E.; Neumann, A.; Pasakarnis, T.; Premaratne, W.A.P.J.; Scherer M.M. Fe(II)-catalyzed recrystallization of goethite revisited. *Environ. Sci. Technol.* **2014**, *48*, 11302-11311.

(80) Kostka, J. E.; Luther, G. W.; Nealson, K. H. Chemical and biological reduction of Mn(III)-pyrophosphate complexes – Potential importance of dissolved Mn(III) as an environmental oxidant. *Geochim. Cosmochim. Acta* **1995**, 59, 885−894.

(81) Nico, P. S.; Zasoki, R. J. Importance of Mn(III) availability on the rate of Cr(III) oxidation on δ-MnO_2. *Environ. Sci. Technol.* **2000**, 36, 3363-3367.

(82) Weaver, R.M.; Hochella, M.F. The reactivity of seven Mn-oxides with Cr^{3+}(aq): A comparative analysis of a complex, environmentally important redox reaction. *Am. Mineralogist* **2003**, 88, 2016-2027.

(83) Simanova, A.A.; Pena, J. Time-resolved investigation of cobalt oxidation by Mn(III)-rich δ-MnO_2 using quick X-ray absorption spectroscopy. *Environ. Sci. Technol.* **2015**, 49, 10867-10876.

(84) Wang, Z.; Xiong, W.; Tebo, B. M.; Giammar, D. E. Oxidative UO_2 dissolution induced by soluble Mn(III). *Environ. Sci. Technol.* **2014**, 48, 289-298.

(85) Tang, Y.Z.; Webb, S.M.; Estes, E.R.; Hansel, C.M. Chromium(III) oxidation by biogenic manganese oxides with varying structural ripening. *Environ. Sci. Processes Impacts*. **2014**, 16, 2127-2136.

(86) Simanova, A.A.; Kwon, K.D.; Bone, S.E.; Bargar, J.R.; Refson, K.; Sposito, G.; Pena, J. Probing the sorption reactivity of the edge surface in birnessite nanoparticles using nickel(II). *Geochim. Cosmochim. Acta* **2015**, 164, 191-204.

(87) Wang Y., Stone A. T. Phosphonate- and carboxylate-based chelating agents that solubilize (hydr)oxide-bound Mn(III). *Environ. Sci. Technol*. **2008**, 42, 4397−4403.

(88) Trouwborst, R. E.; Clement, B. G.; Tebo, B. M.; Glazer, B. T.; Luther, G. W. Soluble Mn(III) in suboxic zones. *Science*. **2006**, 313 (5795), 1955−1957.

(89) Madison, A. S.; Tebo, B. M.; Luther, G.W. Simultaneous determination of soluble manganese(III), manganese(II) and total manganese in natural (pore)waters. *Talanta*. **2011**, 84, 374−381.

(90) Madison, A. S.; Tebo, B. M.; Mucci, A.; Sundby, B.; Luther, G. W. Abundant porewater Mn(III) is a major component of the sedimentary redox system. *Science*. **2013**, 341 (6148), 875−878.

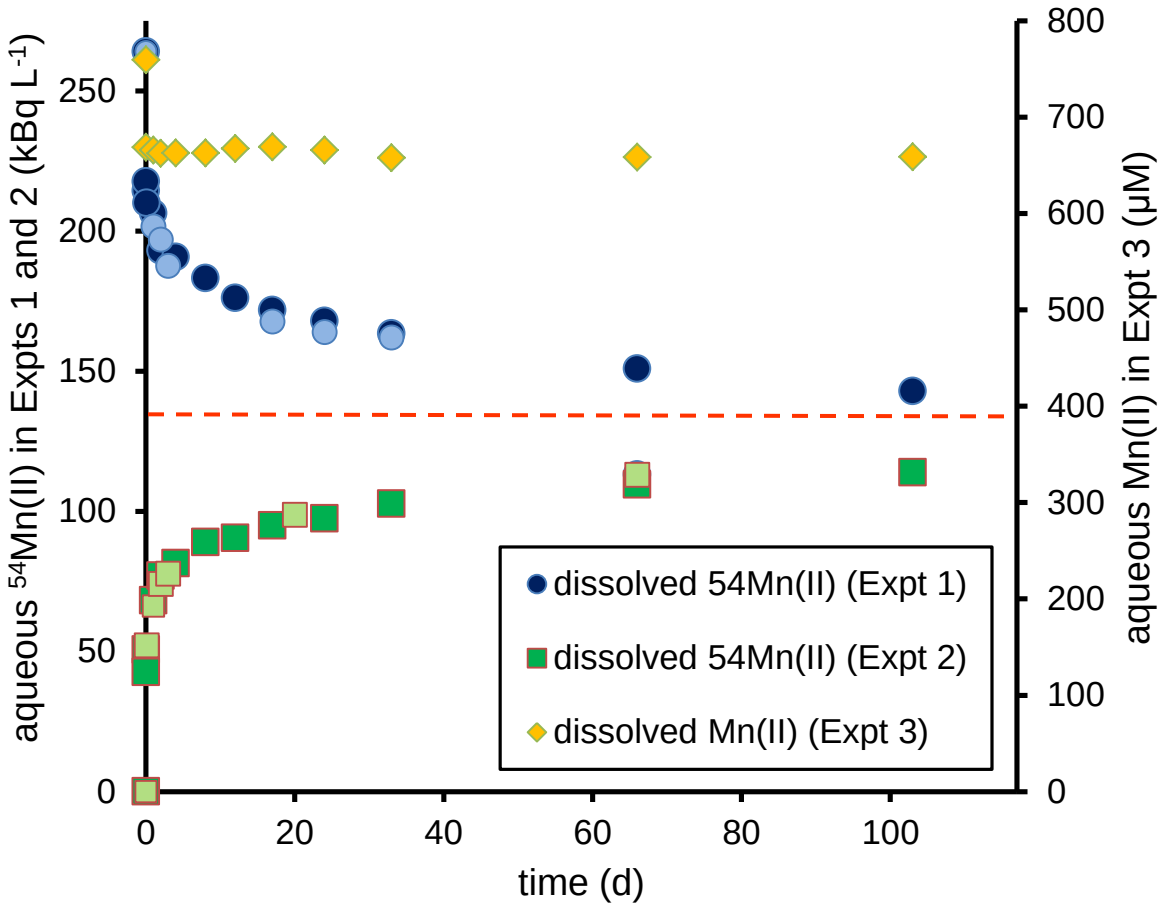

Figure 1. Time-dependencies of the concentrations of dissolved ^{54}Mn(II) ($[^{54}Mn(II)]_{aq}$) in experiments 1 and 2, and of total dissolved Mn(II) ($[Mn(II)]_{aq}$) measured in experiment 3. In experiment 1, aqueous ^{54}Mn(II) was reacted with $MnO_{2(s)}$; in experiment 2, aqueous Mn(II) was reacted with $^{54}MnO_{2(s)}$; experiment 3 involved reaction of aqueous Mn(II) with $MnO_{2(s)}$. Darker and lighter data points in the data series of experiments 1 and 2 represent results from different experiments, and demonstrate the reproducibility of the results. All experiments were conducted under identical conditions, using suspensions with a $MnO_{2(s)}$ particle loading of 530 μM (~0.05 g L^{-1}), a pH of 5.0, and an initial $Mn(II)_{(aq)}$ concentration of 760 μM. The total ^{54}Mn activity in the suspensions of experiments 1 and 2 was 264 kBq L^{-1}. The red dashed line indicates the $[^{54}Mn(II)]_{aq}$ solution level predicted for isotope equilibrium (135 KBq L^{-1}), as explained in the main text.

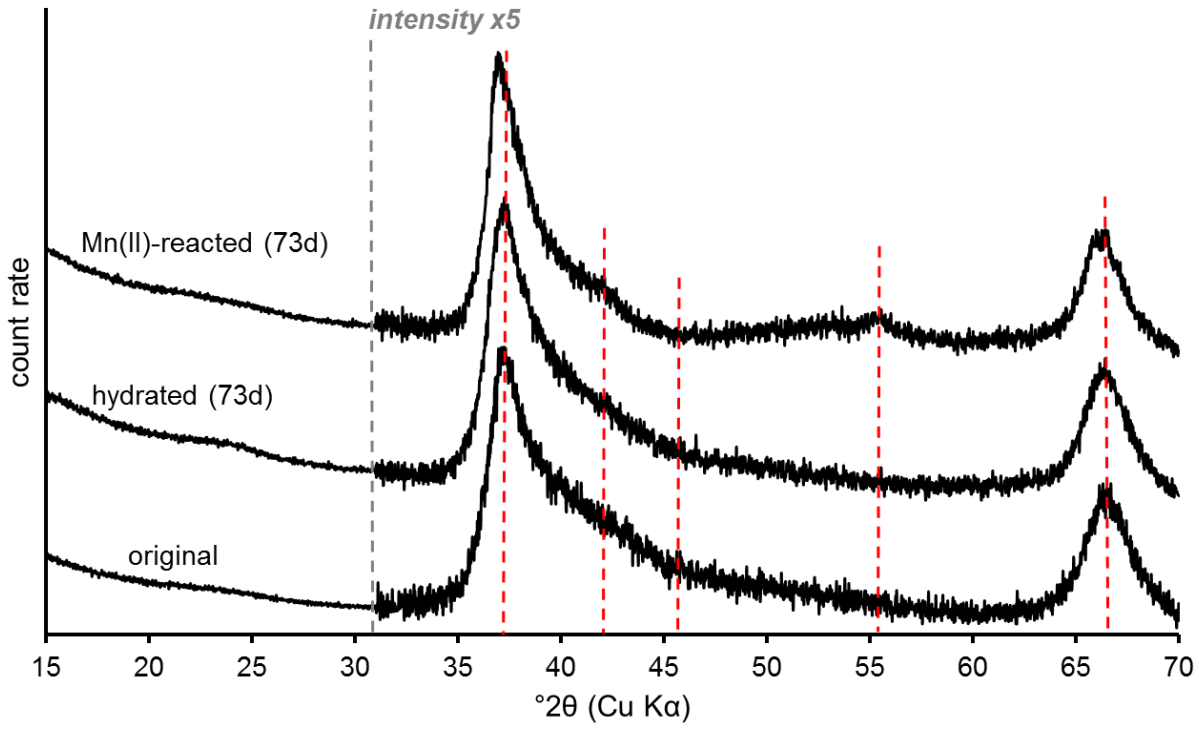

Figure 2. Powder X-ray diffraction (XRD) patterns of: (i) $MnO_{2(s)}$ following 73 d of reaction with 760 µM $Mn(II)_{(aq)}$ at pH 5.0 and a suspension density of 530 µM $MnO_{2(s)}$ (top pattern); (ii) $MnO_{2(s)}$ following hydration at pH 5.0 without Mn(II)(aq) at a suspension density of 530 µM $MnO_{2(s)}$ (middle pattern); and (iii) the $MnO_{2(s)}$ starting substrate (bottom pattern). The regions to the high-angle side of the grey dashed line were scaled by a factor 5. The red dashed lines locate differences in the diffractogram of the Mn(II)-reacted material relative to the original and hydrated control samples as discussed in the main text.

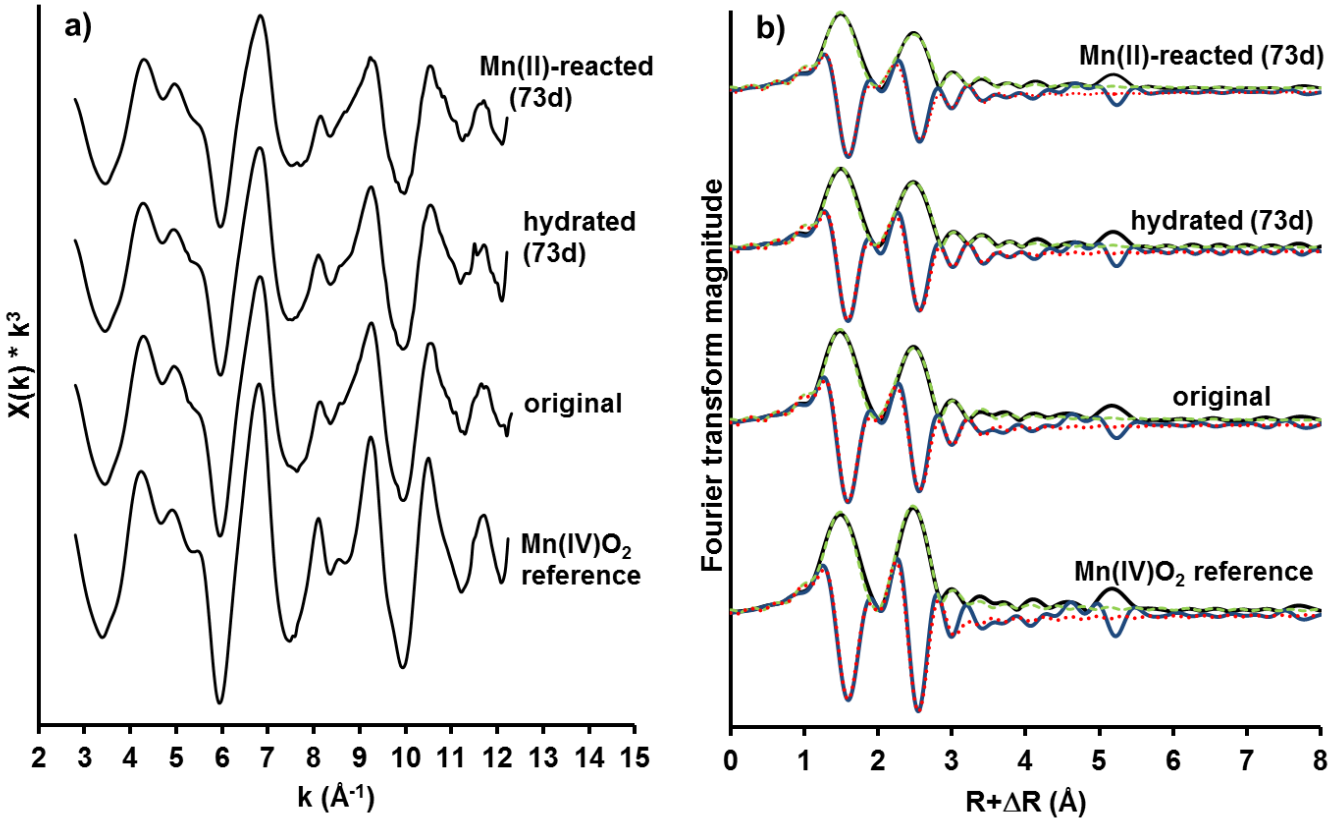

Figure 3. Mn K-edge EXAFS data of the $MnO_{2(s)}$ samples: (a) k^3-weighted χ spectra; and (b) raw and fitted Fourier transforms. The blue and black solid lines in (b) represent the imaginary part and magnitude of the Fourier transforms of the raw spectra, respectively; while the corresponding fits are represented by the green and red dotted lines. The fitting procedure and fit results are summarized in the SI (section 3.3 and Table S1). The $Mn(IV)O_2$ reference is vernadite with an average Mn oxidation state of 4.0, as described in the SI (section 3.2). An overlay of the χ spectra is presented in SI Figure S4 to compare their oscillation patterns and intensities.

TOC art